OPTICA

All-optical nanoscopic spatial control of molecular reaction yields on nanoparticles

Wenbin Zhang,[1,2,3,11] Ritika Dagar,[1,2] Philipp Rosenberger,[1,2] Ana Sousa-Castillo,[4] Marcel Neuhaus,[1] Weiwei Li,[1] Sharjeel A. Khan,[5] Ali S. Alnaser,[5] Emiliano Cortes,[4] Stefan A. Maier,[4,6,7] Cesar Costa-Vera,[8] Matthias F. Kling,[1,2,9,10,12] and Boris Bergues[1,2,*]

[1]*Department of Physics, Ludwig-Maximilians-Universität Munich, D-85748 Garching, Germany*
[2]*Max Planck Institute of Quantum Optics, D-85748 Garching, Germany*
[3]*State Key Laboratory of Precision Spectroscopy, East China Normal University, Shanghai, 200241, China*
[4]*Chair in Hybrid Nanosystems, Nanoinstitute Munich, Königinstrasse 10, Faculty of Physics, Ludwig-Maximilians-Universität Munich, 80539, Munich, Germany*
[5]*Department of Physics, American University of Sharjah, Sharjah, POB26666, United Arab Emirates*
[6]*Department of Physics, Imperial College London, London, SW7 2AZ, UK*
[7]*School of Physics and Astronomy, Monash University, Clayton Victoria 3800, Australia*
[8]*Department of Physics, Escuela Politecnica Nacional, 170525, Quito, Ecuador*
[9]*SLAC National Accelerator Laboratory, Menlo Park, California 94025, USA*
[10]*Applied Physics Department, Stanford University, Stanford, California 94305, USA*
[11]*e-mail: wenbin.zhang@physik.uni-muenchen.de*
[12]*e-mail: kling@stanford.edu*
Corresponding author: boris.bergues@mpq.mpg.de

Molecular adsorbate reactions on nanoparticles play a fundamental role in areas such as nano-photocatalysis, atmospheric, and astrochemistry. They can be induced, enhanced, and controlled by field localization and enhancement on the nanoparticle surface. In particular, the ability to perform highly controlled near-field-mediated reactions is key to deepening our understanding of surface photoactivity on nanosystems. Here, using reaction nanoscopy, we experimentally demonstrate all-optical nanoscopic control of surface reaction yields by tailoring the near fields on nanoparticles with waveform-controlled linear and bicircular two-color laser pulses, respectively. We observe site-selective proton emission from the dissociative ionization of adsorbate molecules on SiO_2 nanoparticles as a function of the polarization and relative phase of the two-color pulses. The angularly resolved close-to-uniform mapping between the surface reaction yields and the measured ion momentum enables the observation and spatial control of molecular reactions on the nanoparticle surface with nanoscopic resolution. The experimental results are modeled and reproduced qualitatively by classical trajectory Monte Carlo simulations. Our work paves the way toward reliable all-optical control of photocatalytic chemical reactions on nanoscale surfaces. © 2022 Optica Publishing Group under the terms of the Optica Open Access Publishing Agreement

1. INTRODUCTION

Due to their unique characteristics, nanostructured materials have a huge potential for applications in a wide range of fields, from physics and chemistry to medicine. For instance, the large surface-to-volume ratio of nanoparticles offers unique capabilities as photocatalysts for chemical reactions [1–3]. Additionally, the nanoscopic surface chemistry and electro-chemistry of structured nanoparticles enable disruptive medical treatments [4] and novel advanced battery technologies [5]. For instance, mesoporous dielectric nanoparticles have been considered as efficient and precise drug delivery agents in targeted cancer therapies [6], while synthesized metal-oxide nanoparticles are capable of enhancing battery performance by optimizing their capacity and cyclability [7]. A key feature of nanomaterials is their characteristic optical response. Under irradiation with light, the localization and enhancement of electromagnetic fields in the vicinity of the nanostructures facilitate various promising applications, including nanofocusing and shadowing [8,9], chemical and biological sensing [10], single-molecule spectroscopy and microscopy [11,12], and nanoscale optoelectronics [13].

Interaction of nanosystems with intense laser pulses permits precision laser machining [14], plasma imaging [15], and the study of nontrivial shock wave formation [16,17]. By tailoring the waveform of the laser pulses, it even becomes possible to generate well-defined optical near fields on the nanostructures that facilitate

the spatiotemporal steering of ultrafast processes at the nanoscale. This ability has been demonstrated with carrier-envelope-phase stabilized few-cycle [18,19] or phase-controlled linear two-color femtosecond pulses [20], by controlling near-field-driven photoelectron emission from dielectric nanospheres [17–22], metal nanotips [23,24], and surface-assembled nanoantennas [25]. In photochemistry, laser-induced near fields can be utilized to induce, enhance, and control molecular adsorbate reactions on the surface of nanoparticles. Both unimolecular and bimolecular photochemical reactions, including deprotonation, proton migration, as well as bond cleavage and bond formation, are generally involved in the molecular adsorbates reactions. The study of those reactions may provide important clues about the surface chemistry of nanoparticles. The recently developed reaction nanoscopy [26], which is based on the three-dimensional (3D) momentum spectroscopy of charged molecular fragments, allows imaging near-field-induced reaction yield distributions on the surface of isolated nanoparticles and their clusters [27]. The technique has recently enabled the observation of anomalous formation of trihydrogen cations from inorganic water molecules on nanoparticles [28]. Despite this progress, coherent control of near-field-mediated molecular adsorbate reactions, which would allow nanoscale spatiotemporal

manipulation of catalytic photochemical reactions on nanoparticles, has not been realized so far. Here, we close this gap and report the experimental demonstration of all-optical nanoscopic spatial control of the reaction yield landscape on the surface of isolated nanoparticles.

The idea behind our experimental approach is to generate spatiotemporally tailored near fields using waveform-controlled linear and bicircular two-color laser pulses. The latter consist of a fundamental wave (FW) that is overlapped with its second harmonic (SH). The synthesized electric fields can be expressed as

$$\varepsilon_{\text{linear}}(t) = \varepsilon_1(t)\cos(\omega t) + \varepsilon_2(t)\cos(2\omega t + \phi_L) \quad (1)$$

and

$$\varepsilon_{\text{bicircular}}(t) = \varepsilon_1(t)[\sin(\omega t)\mathbf{e}_y + \cos(\omega t)\mathbf{e}_z]$$
$$+ \varepsilon_2(t)[\pm\sin(2\omega t + \phi_L)\mathbf{e}_y + \cos(2\omega t + \phi_L)\mathbf{e}_z], \quad (2)$$

respectively, where $\varepsilon_i(t)$ are the fields' envelopes, ω is the carrier frequency of the FW field, and ϕ_L is the relative phase between the FW and SH fields. In the above formula, $\mathbf{e}_{y,z}$ are the unit vectors along the corresponding laboratory axes, and the sign $+/-$ accounts for the bicircular pulses of the same or opposite helicities,
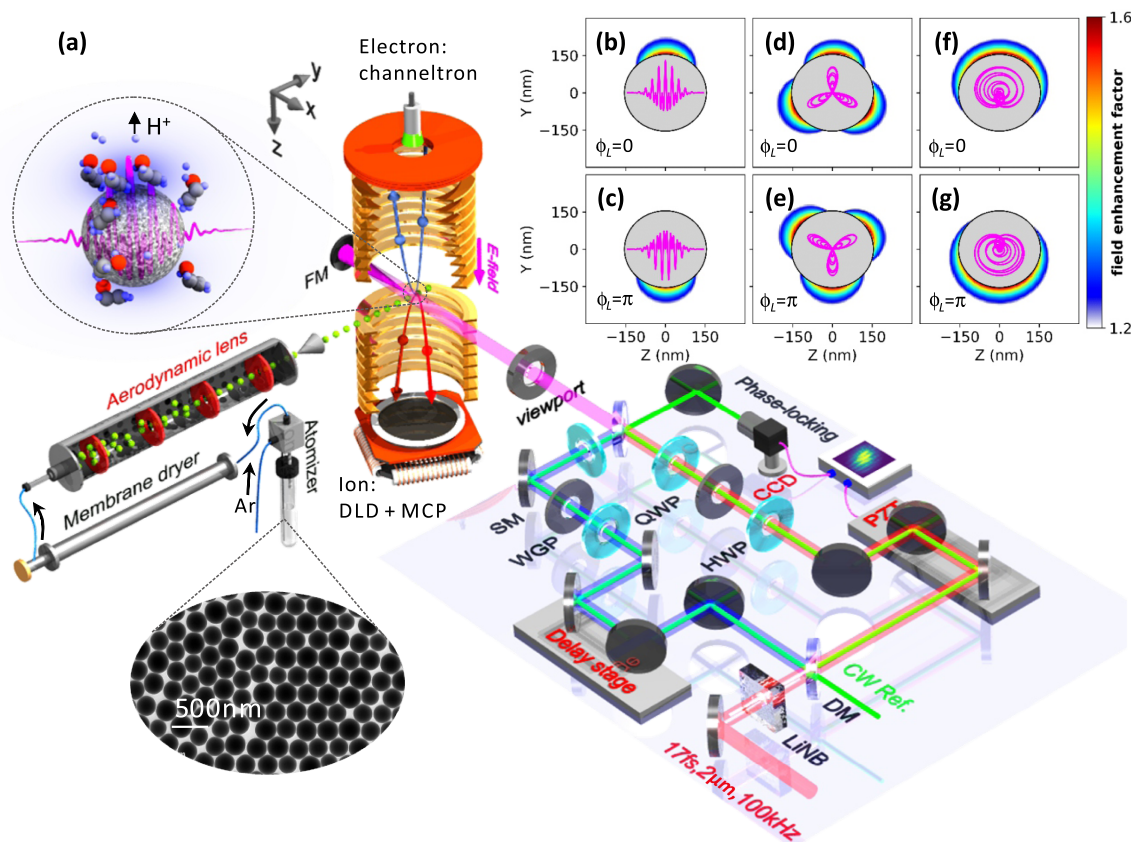

Fig. 1. Experimental scheme. (a) Schematic illustration of the experimental setup showing the reaction nanoscopy and the a phase-locked two-color interferometer. The upper-left inset illustrates the asymmetric proton emission from the surface of nanoparticle driven by a linearly polarized two-color laser pulse. The bottom-left inset shows a transmission electron micrograph (TEM) of 300 nm SiO_2 nanoparticles. DM, dichroic mirror; LiNB, lithium niobate; HWP, half-wave plate; QWP, quarter-wave plate; WGP, wire-grid polarizer; CW, continuous-wave; PZT, piezo-driven translation stage; CCD, charge-coupled device; SM, silver mirror; MCP, microchannel plate; DLD, delay-line anode detector; FM, focusing mirror. (b)–(g) Spatial distribution of the near-field enhancement in the laser polarization plane ($y-z$ plane) for 300 nm SiO_2 nanoparticles driven by (b), (c) linear; (d), (e) counter-rotating; and (f), (g) co-rotating bicircular two-color (2 μm and 1 μm) laser fields with relative phase of 0 and π, respectively, as obtained from finite-difference time-domain (FDTD) simulations (see Supplement 1 for details). The shapes of combined electric fields of the two-color fields for different phases and laser polarizations are illustrated inside of the gray sphere of each figure. The color scale indicates the field enhancement factor.

respectively. The near-field distributions around a single 300 nm silica (SiO_2) nanoparticle tailored by the above driving laser pulses are displayed in Figs. 1(b)–1(g). For linear two-color pulses [Figs. 1(b) and 1(c)], the spatial distribution of the near-field enhancement has a dipole-like shape and oscillates up and down as the relative phase ϕ_L is varied from 0 to π. Thereby, the maximum field enhancement closely follows the direction of the maximum of the driving fields. When switching the polarization of the two-color pulses from linear to bicircular, more exotic phase- and helicity-dependent trefoil [Figs. 1(d) and 1(e)] and semilunar [Figs. 1(f) and 1(g)] near-field patterns emerge. The sensitive dependence of the near-field distribution on the relative phase and polarization of two-color pulses suggest the possibility of site-specific control of near-field-driven molecular adsorbate reactions on the nanoparticle's surface, which we investigate in the present work. More specifically, we use reaction nanoscopy to trace proton emission from dissociative ionization of molecular adsorbates on the surface of SiO_2 nanoparticles, including physisorbed [29] and chemisorbed [30] ethanol molecules from the solvent as well as silanol groups (see Supplement 1). As we will show in the following, the angularly close-to-uniform mapping between the measured proton momentum distributions and the angle-resolved reaction yields landscape on the nanoparticle surface facilitates the observation of surface reactions and their spatial control via the laser phase with nanoscopic resolution.

2. EXPERIMENTAL SCHEME

As schematically illustrated in Fig. 1(a), the measurements were performed in a reaction nanoscope also referred to as Nano-Target Recoil Ion Momentum Spectroscopy (NanoTRIMS) [26], used with two-color laser pulses produced in a phase-locked Mach–Zehnder interferometer. More experimental details can be found in Supplement 1. Briefly, a linearly polarized mid-infrared laser pulse (17 fs, 2 μm, 100 kHz) [31] was frequency doubled in a 1.5-mm-thick lithium niobate (LNB) crystal to generate two-color laser pulses. An active phase-locking system [32] was employed to finely tune the relative phase ϕ_L between the two-color components and also to maintain the stability of the interferometer. The generated phase- and polarization-controlled two-color laser pulse was tightly focused onto a SiO_2 nanoparticle beam inside the NanoTRIMS, using a concave silver mirror ($f = 75$ mm). In reaction nanoscopy, the electrons and ions generated from the nanoparticle-mediated photoreactions are detected in coincidence. Positively charged ion fragments are registered on a time- and position-sensitive detector, facilitating the reconstruction of their full 3D momentum distributions. Electrons are detected using a channeltron electron multiplier on the opposite side of the spectrometer. Since ionization events involving a nanoparticle correlate with a 2 orders of magnitude higher channeltron signal as compared to that from the background gas, the measured electron signal is employed to clearly discriminate molecular ionization and dissociation events occurring on the surface of nanoparticles [26–28].

In the experiment, different ion species, such as H^+, H_2^+, CH_2^+/CH_3^+, and heavier fragments, are generated from the field-induced fragmentation of surface molecules (see Supplement 1). In the following, the most abundant proton signal is used for demonstrating the spatial control of molecular reaction yields on nanoparticles.

3. RESULTS

A. Spatially Selective Proton Emission in Linear Two-Color Pulses

We first demonstrate the directionality control of proton emission from a nanoparticle surface with phase-controlled linearly polarized two-color laser pulses. Figure 2(a) shows the measured phase-integrated proton momentum distributions ($p_x = 0$ plane) obtained from molecular adsorbates on $d = 300$ nm nanoparticles. By gating the events that are coincidently measured with a high electron channeltron signal, the proton signals from background gas ($|p_y| < 35$ a.u.) are efficiently suppressed. As shown in Figs. 2(b) and 2(c), distinct phase-dependent upward and downward oscillations of the proton momentum distributions along the laser polarization direction (the p_y axis) are observed when the relative phase ϕ_L is varied from 0 to π (see Visualization 1 for the animated movie). These observations strongly resemble the up-down switching features of the near-field distributions in a phase-controlled linear two-color pulse [see Figs. 1(b) and 1(c)]. For a more quantitative discussion, we introduce the asymmetry parameter

$$A(\text{KE}, \phi_L) = \frac{Y_{\text{up}}(\text{KE}, \phi_L) - Y_{\text{down}}(\text{KE}, \phi_L)}{Y_{\text{up}}(\text{KE}, \phi_L) + Y_{\text{down}}(\text{KE}, \phi_L)}, \qquad (3)$$

which is a function of the proton kinetic energy (KE) and laser phase ϕ_L. Here, $Y_{\text{up}}(\text{KE}, \phi_L)$ and $Y_{\text{down}}(\text{KE}, \phi_L)$ are the angle-integrated proton yields in the upward ($p_y > 0$) and downward ($p_y < 0$) direction, respectively. The asymmetry maps are shown in Fig. 2(g) for the 300 nm nanoparticle measurement. Note that here the absolute value of ϕ_L is calibrated with the phase-dependent single ionization of the carrier gas of argon atoms under the same experimental conditions. For Ar^+ ions, the probability maxima for the ejection into the positive or negative direction along the polarization axis occur for $\phi_L = 0$ and π, respectively [33], which enables absolute phase calibration. The proton emission from nanoparticles strongly depends on the phase ϕ_L but weakly depends on the KE. As shown in Fig. 2(h), the modulation depth for the asymmetric proton emission from 300 nm nanoparticles is about 90%. From the ϕ_L-dependent asymmetries, it can be seen that protons on the surface of nanoparticles are mostly emitted along the direction of the optical field maximum and closely follow the maximal field enhancement of the near-field distribution. This enables the one-dimensional control of proton emission along the laser polarization direction via the relative phase of linearly polarized two-color laser pulses.

Interestingly, as shown in Fig. 2(h), the phase modulation for the directional proton emission is smaller (~50%) for larger 600 nm nanoparticles. This can be ascribed to the associated field-propagation-induced near-field enhancement on nanoparticles with different sizes [see Figs. 3(a) and 3(f)]. For a nanosphere exposed to laser field, the effect of field propagation on the near-field spatial profiles can be characterized by the Mie parameter [34], i.e., $\rho = \pi d/\lambda$, where d is the sphere diameter and λ is the irradiation wavelength. It is expected that the maximal field enhancement of the near fields exhibits a dipole-like feature along the laser polarization direction when the nanoparticle size is much smaller compared with the wavelength ($\rho \ll 1$), or a forward focusing character along the laser propagation direction when
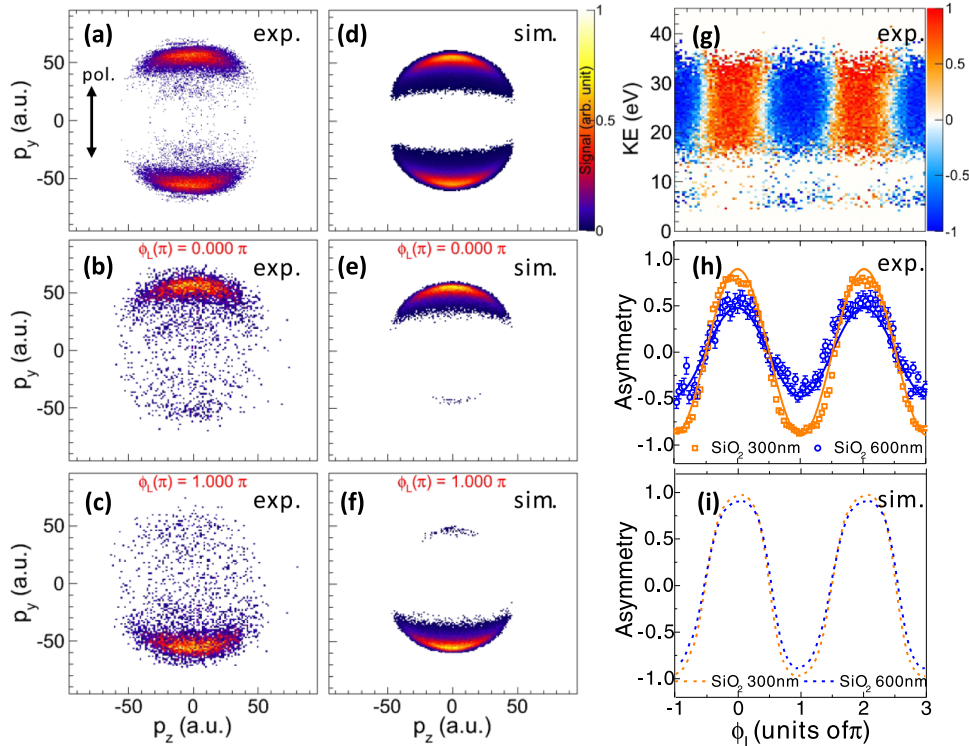
Fig. 2. Proton emission control with linear two-color laser pulses. The nanoparticle-associated proton momentum distributions in the laser polarization plane ($y-z$ plane) obtained from the (a)–(c) experiments and (d)–(f) simulations on 300 nm SiO$_2$ nanoparticles driven by a phase-controlled linearly polarized two-color laser pulse. The laser polarization is along the y axis. The intensities of the spectral components of the linear two-color laser pulses were estimated to be $I_{FW} \sim 2.4 \times 10^{12}$ W/cm^2 and $I_{SH} \sim 6.0 \times 10^{13}$ W/cm^2. The phase-integrated momentum distributions are shown in (a) and (d). The proton momentum distributions at the laser relative phase of (b), (e) $\phi_L = 0$ and (c), (f) $\phi_L = \pi$, respectively. The animated movie of Figs. 2(a)–2(f) can be found in Visualization 1. (g) Measured proton emission asymmetries as a function of the relative phase ϕ_L of the linear two-color pulse and the kinetic energy release (KER) of protons. (h) Measured energy-integrated asymmetry of the proton emission on the surface of 300 nm (orange squares) and 600 nm (blue circles) nanoparticles. The solid curves are the sinusoidal fits of the measured data. (i) Numerically simulated asymmetries of the directional proton emission from 300 nm (orange dashed line) and 600 nm (blue dashed line) nanoparticles.

the Mie parameter is approaching or larger than unity ($\rho \gtrsim 1$) [19,20]. As shown in Figs. 3(b) and 3(g), due to the field propagation effects with different propagation parameters ρ for the two spectral components, the maximal near field for the ω (blue curves) and 2ω (red curves) components nearly overlap near the polar position ($\Theta_f^{xy} = \pm 90°$) for 300 nm particles [see Fig. 3(b)] but differ substantially at the back side of the sphere ($-90° < \Theta_f^{xy} < 90°$) for the 600 nm particles [see Fig. 3(g)]. Here Θ_f^{xy} is defined as $\Theta_f^{xy} = \arctan(p_x/p_y)$. As a result, for 600 nm particles, the smaller spatial overlap of the near-field hot spots, contributed by ω and 2ω components of the two-color pulses, leads to a smaller degree of proton emission phase control ($\sim 50\%$) as compared to that of $\sim 90\%$ for 300 nm particles.

Moreover, the size-dependent near-field deformation can directly be manifested in the measured proton angular distributions [26]. As shown in Figs. 3(d) and 3(i), a comparison of phase-dependent angular distributions Θ_f^{xy} of the proton emitting from 300 and 600 nm particles reveals similar phase-dependent upward and downward yield oscillations but a significant shift of the proton emission direction from nearly $\pm 90°$ to about $\pm 70°$ as particle size increases.

B. Two-Dimensional Control of Proton Emission with Bicircular Two-Color Pulses

We now extend the abovementioned control scheme to more complex bicircular two-color laser pulses to steer the laser-induced near-field maximum in two dimensions, i.e., in the plane spanned by the laser polarization axes. For the bicircular two-color laser pulses, the relative phase $\phi_L = 0$ of the counter- or co-rotating fields is defined as the phase for which one of the three lobes of the trefoil field or the maximum of the semilunar laser field is oriented along the y axis as shown in Figs. 1(d) and 1(f). As revealed in the linear two-color results, the proton ejection direction closely coincides with the maximum of electric field. Therefore, we can accordingly calibrate the measured phase ϕ_L by examining the measured proton angular distributions in the polarization plane. Figures 4(a) and 4(e) display the measured momentum distributions of protons ejected from a $d = 300$ nm nanoparticle and in the polarization plane at $\phi_L = 0$ for a counter- and co-rotating two-color pulse, respectively. Similar to the near-field distributions induced by a bicircular two-color pulse, which have three maxima per cycle for counter-rotating [Figs. 1(d) and 1(e)] or one maximum per cycle for co-rotating [Figs. 1(f) and 1(g)] helicity, a clear trefoil [Fig. 4(a)] and a semilunar [Fig. 4(e)] pattern can be observed in the corresponding proton momentum distributions. The trefoil and semilunar patterns of the proton momentum distributions behave like a rotating fan as the laser phase ϕ_L is varied
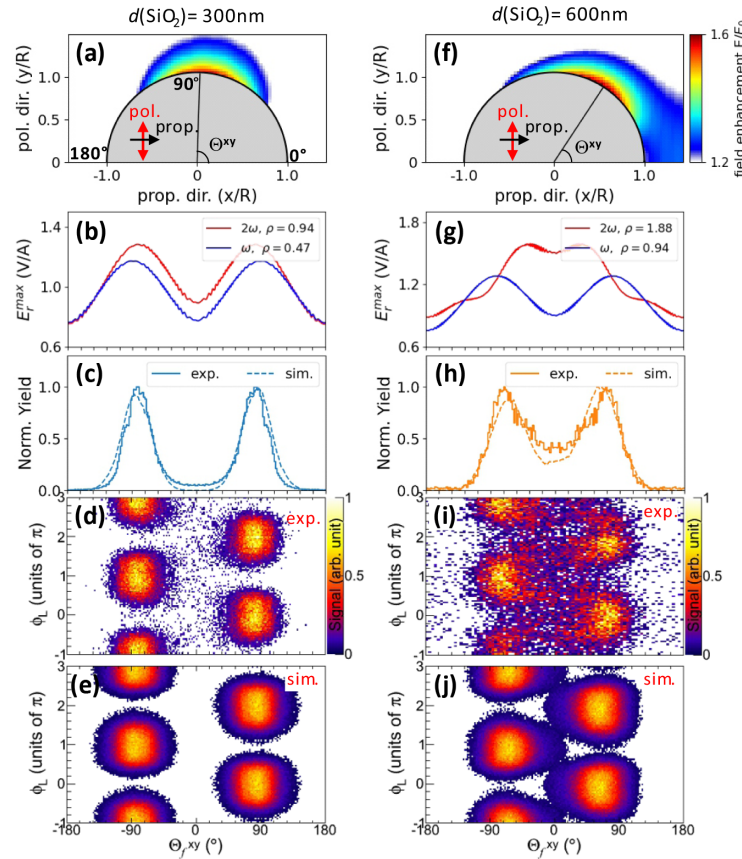
Fig. 3. Near-field propagation effect in phase-controlled proton emission. (a) Calculated spatial distributions of the near-field enhancement on 300 nm SiO$_2$ nanoparticles, in the propagation-polarization plane ($x-y$ plane) of a linearly polarized two-color laser pulse, consisting of fundamental wave at 2 μm (ω) and second-harmonic component at 1 μm (2ω) as obtained from the FDTD simulations. Only the upper-half sphere is shown due to the symmetric distribution along the laser polarization direction. (b) Corresponding angular dependence of the maximum near-field (radial component) for the ω (blue solid curve) and 2ω (red solid curve) components of the two-color laser fields for 300 nm SiO$_2$ spheres. (d) Measured and (e) simulated emission angle Θ_f^{xy} (in the $x-y$ plane) and phase ϕ_L-resolved momentum distribution of protons emitted from the surface of 300 nm SiO$_2$ nanoparticles in linearly polarized two-color laser fields. The corresponding phase-integrated angular distributions Θ_f^{xy} of proton emission are shown in (c), where the solid and dashed lines indicate the experimental and simulation results, respectively. (f)–(j) same as (a)–(e) but for the case of 600 nm nanoparticle.

continuously (see Visualization 2 for the animated movie). This demonstrates two-dimensional spatial control of proton emission on the nanoparticle surface by using bicircular two-color pulses. The slight phase-independent asymmetry of the measured proton distribution along the z axis mainly originates from a reduction of the detector efficiency for ions arriving later within a mass peak and hitting the detector within the recovery time of the microchannel plate (MCP). The effect is most pronounced for protons, which are the most abundant ion species emitted from nanoparticle surface in our experiment and are mainly visible when the ions are emitted along the z axis (time-of-flight direction).

For a more quantitative analysis of the two-dimensional proton emission control, we define the asymmetry parameter

$$A(p_y, p_z, \phi_L) = \frac{Y(p_y, p_z, \phi_L) - Y(p_y, p_z, \phi_L + \pi)}{Y(p_y, p_z, \phi_L) + Y(p_y, p_z, \phi_L + \pi)}, \quad (4)$$

where $Y(p_y, p_z, \phi_L)$ is the measured proton yield at momentum $\boldsymbol{p} = (p_y, p_z)$ and the relative phase ϕ_L of the bicircular two-color pulse. For a given ϕ_L, the asymmetry parameter is positive if protons are preferentially emitted with an angle $\Theta_f^{yz} = \arctan(p_y/p_z)$ and negative if protons are preferentially emitted with an angle $\Theta_f^{yz} + 180°$. Figures 4(b) and 4(f) display

the corresponding two-dimensional asymmetry pattern of the proton momentum distributions in the $y-z$ plane for counter- and co-rotating two-color pulses, respectively (see Visualization 3 for the animated movie). Interestingly, although the two-color laser pulses with different helicities have the same combined field intensity in the experiment, the measured asymmetry contrast in co-rotating fields [∼75% in Fig. 4(f)] is overall larger than that in counter-rotating fields [∼30% in Fig. 4(b)]. We note that a similar spatial control is expected for nanoparticles with a diameter larger than 300 nm as long as the field-propagation effects are small enough. For instance, the field-propagation effect is already noticeable in the case of 600 nm nanoparticles. However, since the extent of the propagation effect only depends on the particle properties and the laser wavelength but not on the polarization of the electric field, we expect that the phase control demonstrated in the linear two-color experiment (see Fig. 3) could also be achieved in the bicircular two-color case for 600 nm particles.

C. Theoretical Modeling

To unveil the mechanism behind the all-optical control of proton emission on the surface of nanoparticles, we performed
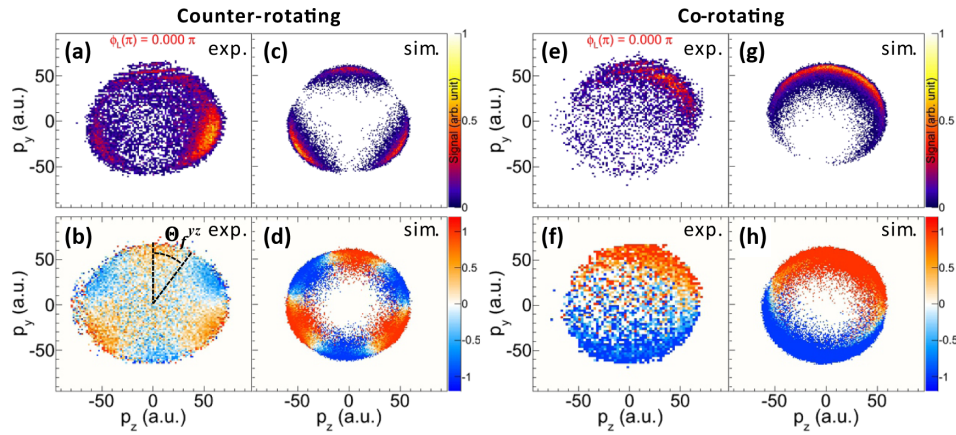
Fig. 4. Proton emission control with bicircular two-color laser pulses. The (a), (e) experimentally measured and (c), (g) numerically simulated momentum distributions of protons emitting from the surface of 300 nm nanoparticles in (p_y, p_z) space at $\phi_L = 0$ of a (a), (c) counter- and (e), (g) co-rotating bicircular two-color pulse. The corresponding two-dimensional asymmetry pattern of the spatially selective proton emission obtained from experiments and simulations are shown in (b), (f) and (d), (h), respectively. The proton emission angle Θ_f^{yz} is indicated by the black dashed lines in (b). The intensities of the spectral components of the bicircular two-color laser pulses were estimated to be $I_{FW} \sim 4.0 \times 10^{12}$ W/cm^2 and $I_{SH} \sim 1.0 \times 10^{14}$ W/cm^2. The animated movie of the figures can be found in Visualization 2 and Visualization 3.

electrostatic classical trajectory Monte Carlo (CTMC) simulations [27]. The general scenario of proton dynamics on the surface of a nanoparticle can be understood as follows. Initially, electrons are released from a nanoparticle by the strong laser pulses, leading to an inhomogeneous distribution of positive charges on the nanoparticle surface, which correlates with the laser-induced near-field enhancement. During the interaction with the laser pulse, molecules on the nanoparticle surface may undergo dissociative ionization, whereby protons emitted in the process are repelled from the nanoparticle by the electrostatic field of the positively charged surface. In the model, it is assumed that the protons are released with zero initial momentum, and the subsequent proton dynamics are dominated by electrostatic interactions with the charged nanoparticle surface. Furthermore, the Coulomb interactions between the fast escaping electrons and the ions ejected from the nanoparticle are assumed to have a negligible effect on the final proton momenta. In simulations, the spatial distribution of static and positive point charges on the nanoparticle surface is calculated using a quasi-static ionization rate [35] obtained from the two-color laser-field-induced near-field enhancement. The initial positions of protons on the surface are sampled from the calculated spatial probability distribution for molecular dissociative ionization. The protons are then propagated classically in the electrostatic field to obtain final 3D momentum spectra. More simulation details can be found in Supplement 1.

As shown in Figs. 2(d)–2(f), the momentum distributions of protons emitted from nanoparticles driven by linearly polarized two-color pulses as well as the features of the two-color phase dependence are qualitatively reproduced by the CTMC simulations for the experimental parameters. Moreover, the simulation results for 300 nm and 600 nm particles also well reproduce the characteristics of the field-propagation effects on the angular distributions as shown in Figs. 3(c), 3(h) (dashed lines) and Figs. 3(e), 3(j), respectively. We note that although the trend is qualitatively reproduced for the calculated asymmetry parameter shown in Fig. 2(i), the amplitude difference between the 300 nm (orange dashed curve) and 600 nm (blue dashed curve) particles is less pronounced than in the measurement, which we attribute to the

simplicity of the model. Nevertheless, the qualitative agreement between the simulations and experimental observations for the two main characteristics of the asymmetry, i.e., the preferential proton emission along the maximum of the asymmetric optical fields as well as the somewhat higher asymmetry amplitude for smaller nanoparticles, is remarkable. Most importantly, our theoretical model also qualitatively reproduces the phase-dependent trefoil and semilunar structures and asymmetries in proton momentum distributions measured with counter- and co-rotating bicircular two-color laser pulses as shown in Figs. 4(c), 4(d) and Figs. 4(g), 4(h), respectively.

4. DISCUSSION

Previous work on the optical control of particle emission dynamics from laser–nanoparticle interaction has concentrated on electron emission from the nanosystems [18–25]. Therein, the controllable, very fast photoemission is steered by the combined fields near the nanoparticle surface, i.e., the dielectrically enhanced near field induced by incident laser pulses and the surface trapping potential produced by released electrons and residual ions [18,19,36,37]. In contrast, in the present study on ion emission, the motion of the much heavier protons is mainly driven by the repulsive Coulomb force from the positively charged nanoparticle. Tailoring the surface near field by phase-controlled linear or bicircular two-color laser pulses enables generating well-defined anisotropic charge distributions on the nanoparticle surface, which in turn allows manipulation of the charge-driven directional proton emission from the surface. In contrast to the electron emission for which the directionality is merely conserved for near-cutoff electrons [18–20], the spatially selective, phase- and polarization-dependent proton emission observed in the present study is seen for the majority of the protons emitted from the nanoparticle. Thus, the proton emission can serve as a sensitive probe for the observation and manipulation of local reaction yields on the nanoparticle surface.

In the following, we discuss the precision of the spatial control of surface reaction yields that is achieved with our method. Before addressing this point, it is instructive to investigate the mapping relation between the initial dissociation yield landscape
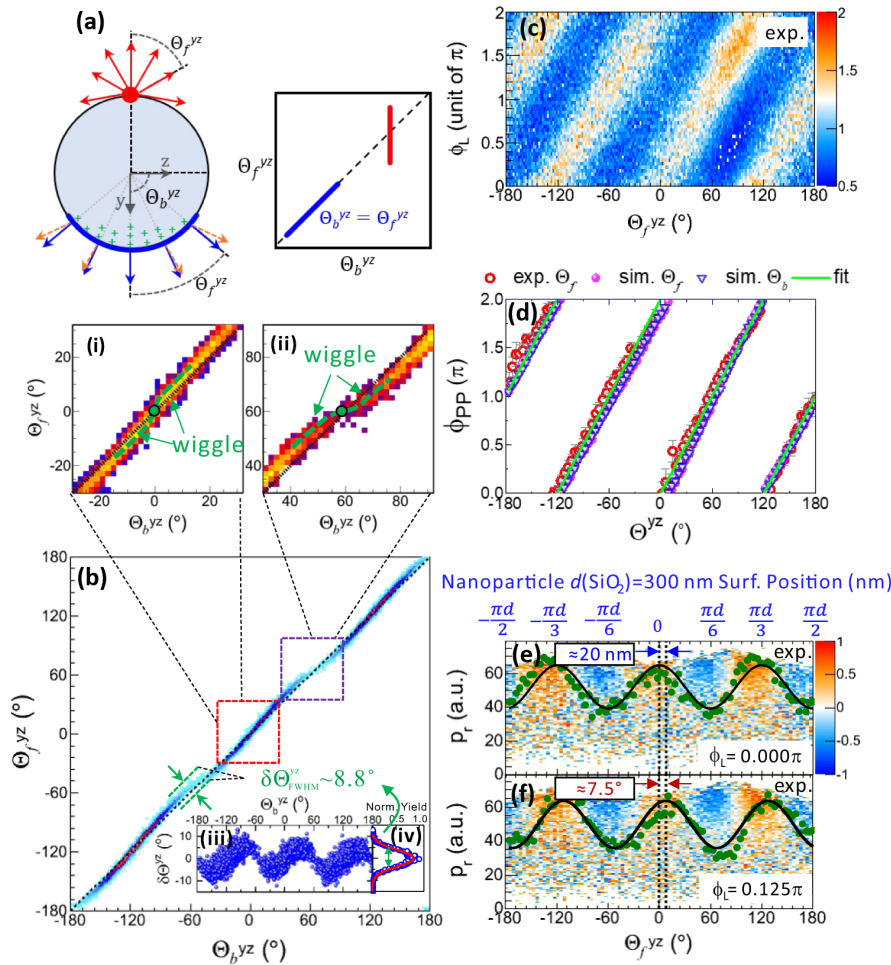
Fig. 5. Nanoscopic spatial control of proton emission on nanoparticle surfaces. (a) Schematic illustration of correlation characteristics between birth angle Θ_b^{yz} and final angle Θ_f^{yz} defined via the projections of birth position and final momentum vector on the $y-z$ and p_y-p_z planes, respectively, for undirected (red) and radial (blue) emission. (b) Correlation plot for the birth angle Θ_b^{yz} and final angle Θ_f^{yz} obtained from simulations of proton emission on a 300 nm nanoparticle driven by a counter-rotating bicircular two-color pulse at $\phi_L = 0$. The inset (i) and (ii) show the enlarged correlation map for birth angle between $-30°$ to $30°$ and $30°$ to $90°$, respectively. The birth-angle-dependent and birth-angle-integrated distributions of angle difference $\delta\Theta^{yz}$ between birth and final angle for each proton trajectory are shown in the insets (iii) and (iv), respectively. (c) Normalized 2D spectra of phase-dependent proton final angle distribution, i.e., Θ_f^{yz} versus ϕ_L, measured using counter-rotating bicircular two-color pulses. (d) Retrieved phase-of-phase ϕ_{PP} spectra for the proton emission angle Θ_f^{yz} and birth angle Θ_b^{yz} obtained from experiments (red open circles) and simulations (purple solid circles for Θ_f^{yz} and blue open triangles for Θ_b^{yz}). The green solid lines are the fits of the retrieved data points with linear functions of a same slope of $2\pi/120°$ and different angle cutoff of Θ^{yz} at $\phi_{PP} = 0$. (e),(f) The measured two-dimensional asymmetry patterns of proton momentum distributions in polar coordinates of the (p_y, p_z) plane, i.e., p_r versus Θ_f^{yz}, for a phase ϕ_L of (e) 0 and (f) 0.125π, respectively. The greed solid circles show the momentum-integrated proton emission angular distributions and were fitted with sinusoidal functions (black solid curves).

on the surface and the measurable final proton momentum distributions using reaction nanoscopy [26]. For this purpose, we analyze the correlation between the angle-resolved directionality of proton generation and the final emission on the nanoparticle surface. A schematic illustration of the correlation between the birth angle (Θ_b^{yz}) and final emission angle (Θ_f^{yz}) is shown in Fig. 5(a). Undirected proton emission from a narrow birth angle region but with a broad distribution of final angles will appear as a vertical feature in the angle-correlation plot [marked in red in right panel of Fig. 5(a)]. In contrast, a concentration of trajectories on the diagonal [marked in blue in the right panel of Fig. 5(a)], i.e., $\Theta_b^{yz} = \Theta_f^{yz}$, indicates radial emission, which allows a direct mapping between the emission and birth angle [37]. Figure 5(b) shows the simulated correlation plot of the birth and final angle of the proton emission driven by a counter-rotating bicircular

two-color laser pulse at $\phi_L = 0$. In the case of radial emission, the angle-correlation distribution in principle should strictly follow the black dashed diagonal line in the correlation plot. However, as displayed on the enlarged correlation map for angles between $-30°$ to $30°$ [inset (i) of Fig. 5(b)] and $30°$ to $90°$ [inset (ii) of Fig. 5(b)], angle-dependent wiggle structures (depicted by green dashed lines) can be observed near the birth surface positions with maximum ($\Theta_b^{yz} = 0°$) and minimal ($\Theta_b^{yz} = 60°$) field enhancement. This can be ascribed to inhomogeneous charge distributions induced by the near field on the nanoparticle surface. As illustrated in Fig. 5(a), the closer the surface position nears the points of maximum field enhancement (hot spots), the more positive charges (green plus symbols) can be generated due to the higher field intensity. For the protons born near the hot spots, the radial emission prevails

because of the high symmetry of the local charge distribution, leading to a one-to-one mapping between birth and final angles. For the protons created at the surface positions away from the hot spot, due to the additional Coulomb force from the higher local charge at the hot spots, the actual final emission direction will be deflected to a larger angle [orange dashed arrows in Fig. 5(a)] as compared to the angle expected for radial emission alone [black solid arrows in Fig. 5(a)]. To quantify the deviations between the birth and final angle, we calculated their angle difference, i.e., $\delta\Theta^{yz} = \Theta_f^{yz} - \Theta_b^{yz}$ for each proton trajectory. The scatter plot of $\delta\Theta^{yz}$ as a function of the birth angle is shown in inset (iii) of Fig. 5(b). By fitting the angle-integrated $\delta\Theta^{yz}$ distributions shown in inset (iv), a full width half-maximum (FWHM) of $\delta\Theta_{\text{FWHM}}^{yz} \sim 8.8°$ was obtained. It implies a considerably small mean value of angle deviation of 4.4° for the angle-to-angle mapping by considering the left and right deviations from the diagonal. With this, despite the existence of the small wiggle structures in the correlation map, the overall distributions of the angle correlation [Fig. 5(b)] exhibit a nearly diagonal shape with an angle correlation coefficient of ∼0.997. This suggests a near-one-to-one mapping between birth and final angle, which is equivalent to the mapping between birth position and final angular distribution of protons emitted from the nanoparticle surface.

It is worth comparing the presented mapping to that reported using rescattered electrons near their energetic cutoff [18–20,37]. Rescattered electrons are prone to having a wider distribution resulting from the collisional dynamics and that drastically decreases in yield toward the cutoff. This results in a significantly lower correlation between birth position and final emission angles, which is quickly translated into a non-correlated emission at lower photoelectron energies. In contrast, for the emission of the heavier protons, the birth-to-final angle correlation is orders of magnitude larger and independent of the ion energy.

The high resolution of spatial control can be assessed by inspecting the phase-dependent variation of emission angle. Figure 5(c) shows the measured ϕ_L-dependent angular distribution of protons emitted in the (p_y, p_z) plane of a counter-rotating bicircular two-color laser pulse, which is normalized as

$$Y_{\text{Norm}}(\Theta_f^{yz}, \phi_L^i) = \frac{Y(\Theta_f^{yz}, \phi_L^i)}{\frac{1}{N}\sum_{\phi_L^i=0}^{\phi_L^N=2\pi} Y(\Theta_f^{yz}, \phi_L^i)}, \qquad (5)$$

where $Y(\Theta_f^{yz}, \phi_L^i)$ is the collected proton yields at final emission angle Θ_f^{yz} laser phase ϕ_L, and N is the total number of scanning steps of the laser phase over 2π. The diagonal structures indicate the rotation of proton momentum lobes with increasing laser phase. To quantitatively extract the mapping relation between the continuously varied relative phase and the proton emission angle, we retrieved the "phase of the phase" (PP) spectra ϕ_{PP}, by fitting a cosine function $Y_{\text{Norm},f}(\phi_L) = Y_0 + A_0 \cos(\phi_L + \phi_{\text{PP}})$ for each angle Θ_f^{yz}. Here Y_0 is the background count, A_0 is the phase contrast, and ϕ_{PP} represents the changes of laser phase with respect to $\phi_L = 0$. As shown in Fig. 5(d), when the emission angle Θ_f^{yz} varies by 360°, the phase ϕ_{PP} changes by 6π in total. This corresponds to a proton emission angle that rotates from −180° to 180° when varying the relative phase ϕ_L from 0 to 6π. The retrieved ϕ_{PP} values for the proton birth (blue open triangles) and final angle (red solid circles) obtained from simulations are also shown in Fig. 5(d). The green solid lines are the fits of the retrieved data points of ϕ_{PP} using linear functions of a same slope of $6\pi/360°$ but different

angle cutoff at $\phi_{\text{PP}} = 0$. The quantitative agreement between the experiments, simulations, and the fitted lines indicate that the proton birth angle can be controlled via the laser phase by means of the close-to-uniform mapping $\Theta_b^{yz}(\phi_L) = (360°/6\pi)\phi_L - 180°$ between the phase ϕ_L and the birth angle Θ_b^{yz} with the units being radian and degree, respectively.

More importantly, the phase control of the birth angle on a nanosphere can directly be translated to the spatial birth position control on the nanoparticle surface by using the formula $S_R^{yz}(\phi_L) = \pi[\Theta_b^{yz}(\phi_L)/360°]d$, where d is the nanosphere diameter. Within the laser polarization plane of a counter-rotating bicircular two-color laser pulse, when laser phase ϕ_L varies by 6π, the proton birth position on the surface can be changed from $-\pi d/2$ to $\pi d/2$. Therefore, by combining the angle-to-angle, angle-to-phase, and phase-to-position mapping relations, the spatial control of the molecular reaction yields on the nanoparticle surface via laser phase can be implemented with nanoscopic resolution that only depends on the nanoparticle's diameter d and the step size of the adjustable laser phase ϕ_L. Figures 5(e) and 5(f) show the measured two-dimensional asymmetry pattern of the proton momentum distribution in polar coordinates of the (p_y, p_z) plane, i.e., p_r versus Θ_f^{yz} for different phases of a counter-rotating pulse. The corresponding momentum-integrated angular distributions (green dots) are fitted with sinusoidal functions (black lines). As indicated by the black dashed lines, an angle shift of 7.5° of the near-field hot spots can be observed when the phase ϕ_L is varied from 0 to 0.125π. As deduced from the phase-to-position mapping law, this is equivalent to the steering of the proton birth position by $S_R^{yz} \sim 20$ nm on the surface of a $d = 300$ nm nanoparticle spanned by the laser polarization plane. Considering the angular resolution of ∼4.4° determined by mean value of the angle deviation between the birth and final angle, the spatial resolution for the surface position control can be deduced as ∼11 nm for the 300 nm particles.

5. CONCLUSION

In conclusion, using reaction nanoscopy, we have demonstrated all-optical, one- and two-dimensional spatial control of molecular reaction yields on the surface of isolated SiO_2 nanoparticles. This was achieved by tailoring the near fields using waveform-controlled linear and bicircular two-color laser pulses, respectively. Our experimental observations of phase- and polarization-dependent directional proton emission are corroborated by semiclassical simulations based on strong field ionization in near fields and static charge interactions. By systematically tuning the birth angle of ionic fragments via the bicircular field, we establish an essentially uniform mapping between the initial birth position on the nanoparticle and the final momentum of the ionic fragment. This enables the observation of molecular adsorbate reactions and their spatial control on the nanoparticle surface with nanoscopic resolutions. The all-optical control scheme, demonstrated here for isolated nanospheres, is expected to be applicable to a wide class of more complex isolated and surface-based nanosystems. Our results pave the way toward the all-optical manipulation of catalytic photochemical reactions on the surface of structured nanoparticles.

Disclosures. The authors declare no conflicts of interest.

Data availability. The data that support the findings of this study are available from the corresponding author upon reasonable request.

Supplemental document. See Supplement 1 for supporting content.

REFERENCES

1. M. Murdoch, G. Waterhouse, M. Nadeem, J. Metson, M. Keane, R. Howe, J. Llorca, and H. Idriss, "The effect of gold loading and particle size on photocatalytic hydrogen production from ethanol over Au/TiO₂ nanoparticles," Nat. Chem. **3**, 489–492 (2011).
2. Q. Xiang, J. Yu, and M. Jaroniec, "Synergetic effect of MoS₂ and graphene as cocatalysts for enhanced photocatalytic H₂ production activity of TiO₂ nanoparticles," J. Am. Chem. Soc. **134**, 6575–6578 (2017).
3. S. Wu and H.-J. Butt, "Near-infrared photochemistry at interfaces based on upconverting nanoparticles," Phys. Chem. Chem. Phys. **19**, 23585–23596 (2017).
4. A. M. Pekkanen, M. R. Dewitt, and M. N. Rylander, "Nanoparticle enhanced optical imaging and phototherapy of cancer," J. Biomed. Nanotechnol. **10**, 1677–1712 (2014).
5. Y. Sun, N. Liu, and Y. Cui, "Promises and challenges of nanomaterials for lithium-based rechargeable batteries," Nat. Energy **1**, 16071 (2016).
6. V. Mamaeva, C. Sahlgren, and M. Lindén, "Mesoporous silica nanoparticles in medicine-recent advances," Adv. Drug Deliv. Rev. **65**, 689–702 (2013).
7. F. Prado, H. Andersen, M. Taeño, J. P. Mæhlen, J. Ramírez-Castellanos, D. Maestre, S. Karazhanov, and A. Cremades, "Comparative study of the implementation of tin and titanium oxide nanoparticles as electrodes materials in Li-ion batteries," Sci. Rep. **10**, 5503 (2020).
8. R. Signorell, M. Goldmann, B. Yoder, A. Bodi, E. Chasovskikh, D. Lang, and L. Luckhaus, "Nanofocusing, shadowing, and electron mean free path in the photoemission from aerosol droplets," Chem. Phys. Lett. **658**, 1–6 (2016).
9. D. K. Gramotnev and S. I. Bozhevolnyi, "Nanofocusing of electromagnetic radiation," Nat. Photonics **8**, 13–22 (2014).
10. J. Becker, A. Trügler, A. Jakab, U. Hohenester, and C. Sönnichsen, "The optimal aspect ratio of gold nanorods for plasmonic bio-sensing," Plasmonics **5**, 161–167 (2010).
11. S. Nie and S. Emory, "Probing single molecules and single nanoparticles by surface-enhanced Raman scattering," Science **275**, 1102–1106 (1997).
12. M. T. Hassan, "Attomicroscopy: from femtosecond to attosecond electron microscopy," J. Phys. B **51**, 032005 (2018).
13. J. Schoetz, Z. Wang, E. Pisanty, M. Lewenstein, M. F. Kling, and M. F. Ciappina, "Perspective on petahertz electronics and attosecond nanoscopy," ACS Photon. **6**, 3057–3069 (2019).
14. K. M. Ahmmed, C. Grambow, and A. M. Kietzig, "Fabrication of micro/nano structures on metals by femtosecond laser micromachining," Micromachines **5**, 1219–1253 (2014).
15. D. D. Hickstein, F. Dollar, J. L. Ellis, K. Schnitzenbaumer, K. E. Keister, G. Petrov, C. Ding, B. Palm, J. Gaffney, M. Foord, S. Libby, G. Dukovic, J.

16. Jimenez, H. Kapteyn, M. Murnane, and W. Xiong, "Mapping nanoscale absorption of femtosecond laser pulses using plasma explosion imaging," ACS Nano **8**, 8810–8818 (2014).
16. D. D. Hickstein, F. Dollar, J. A. Gaffney, M. E. Foord, G. M. Petrov, B. B. Palm, K. E. Keister, J. L. Ellis, C. Ding, S. B. Libby, J. L. Jimenez, H. C. Kapteyn, M. M. Murnane, and W. Xiong, "Observation and control of shock waves in individual nanoplasmas," Phys. Rev. Lett. **112**, 115004 (2014).
17. F. Sun, H. Li, S. Song, F. Chen, J. Wang, Q. Qu, C. Lu, H. Ni, B. Wu, H. Xu, and J. Wu, "Single-shot imaging of surface molecular ionization in nanosystems," Nanophotonics **10**, 2651–2660 (2021).
18. S. Zherebtsov, T. Fennel, J. Plenge, *et al.*, "Controlled near-field enhanced electron acceleration from dielectric nanospheres with intense few-cycle laser fields," Nat. Phys. **7**, 656–662 (2011).
19. F. Süßmann, L. Seiffert, S. Zherebtsov, V. Mondes, J. Stierle, M. Arbeiter, J. Plenge, P. Rupp, C. Peltz, A. Kessel, S. A. Trushin, B. Ahn, D. Kim, C. Graf, E. Rühl, M. F. Kling, and T. Fennel, "Field propagation-induced directionality of carrier-envelope phase-controlled photoemission from nanospheres," Nat. Commun. **6**, 7944 (2015).
20. Q. Liu, S. Zherebtsov, L. Seiffert, *et al.*, "All-optical spatio-temporal control of electron emission from SiO₂ nanospheres with femtosecond two-color laser fields," New J. Phys. **21**, 073011 (2019).
21. L. Seiffert, Q. Liu, S. Zherebtsov, *et al.*, "Attosecond chronoscopy of electron scattering in dielectric nanoparticles," Nat. Phys. **13**, 766–770 (2017).
22. Q. Liu, L. Seiffert, F. Süßmann, *et al.*, "Ionization-induced subcycle metallization of nanoparticles in few-cycle pulses," ACS Photon. **7**, 3207–3215 (2020).
23. M. Krüger, M. Schenk, and P. Hommelhoff, "Attosecond control of electrons emitted from a nanoscale metal tip," Nature **475**, 78–81 (2011).
24. G. Herink, D. R. Solli, M. Gulde, and C. Ropers, "Field-driven photoemission from nanostructures quenches the quiver motion," Nature **483**, 190–193 (2012).
25. P. Dombi, A. Hörl, P. Rácz, I. Márton, A. Trügler, J. Krenn, and U. Hohenester, "Ultrafast strong-field photoemission from plasmonic nanoparticles," Nano Lett. **13**, 674–678 (2013).
26. P. Rupp, C. Burger, N. G. Kling, M. Kübel, S. Mitra, P. Rosenberger, T. Weatherby, N. Saito, J. Itatani, A. S. Alnaser, M. B. Raschke, E. Rühl, A. Schlander, M. Gallei, L. Seiffert, T. Fennel, B. Bergues, and M. Kling, "Few-cycle laser driven reaction nanoscopy on aerosolized silica nanoparticles," Nat. Commun. **10**, 4655 (2019).
27. P. Rosenberger, P. Rupp, R. Ali, M. S. Alghabra, S. Sun, S. Mitra, S. A. Khan, R. Dagar, V. Kim, M. Iqbal, J. Schötz, Q. Liu, S. K. Sundaram, J. Kredel, M. Gallei, C. Vera, B. Bergues, A. Alnaser, and M. F. Kling, "Near-field induced reaction yields from nanoparticle clusters," ACS Photon. **7**, 1885–1892 (2020).
28. M. S. Alghabra, R. Ali, V. Kim, M. Iqbal, P. Rosenberger, S. Mitra, R. Dagar, P. Rupp, B. Bergues, D. Mathur, M. Kling, and A. Alnaser, "Anomalous formation of trihydrogen cations from water on nanoparticles," Nat. Commun. **12**, 3839 (2021).
29. J. Karnes, E. Gobrogge, R. Walker, and I. Benjamin, "Unusual structure and dynamics at silica/methanol and silica/ethanol interfaces—a molecular dynamics and nonlinear optical study," J. Phys. Chem. B **120**, 1569–1578 (2016).
30. S. Björklund and V. Kocherbitov, "Alcohols react with MCM-41 at room temperature and chemically modify mesoporous silica," Sci. Rep. **7**, 9960 (2017).
31. M. Neuhaus, H. Fuest, M. Seeger, J. Schötz, M. Trubetskov, P. Russbueldt, H. Hoffmann, E. Riedle, Z. Major, V. Pervak, M. F. Kling, and P. Wnuk, "10 W CEP-stable few-cycle source at 2 μm with 100 kHz repetition rate," Opt. Express **26**, 16074–16085 (2018).
32. W. Zhang, H. Li, K. Lin, P. Lu, X. Gong, Q. Song, Q. Ji, J. Ma, H. Li, H. Zeng, F. He, and J. Wu, "Photon-number-resolved asymmetric dissociative single ionization of H₂," Phys. Rev. A **96**, 033405 (2017).
33. J. Wu, A. Vredenborg, L. P. H. Schmidt, T. Jahnke, A. Czasch, and R. Dörner, "Comparison of dissociative ionization of H₂, N₂, Ar₂, and CO by elliptically polarized two-color pulses," Phys. Rev. A **87**, 023406 (2013).
34. G. Mie, "Beiträge zur optik trüber medien, speziell kolloidaler metallösungen," Ann. Phys. **330**, 377–445 (1908).
35. M. V. Ammosov, N. B. Delone, and V. P. Krainov, "Tunnel ionization of complex atoms and of atomic ions in an alternating electromagnetic field," Sov. Phys. JETP **64**, 1191–1194 (1986).

36. L. Seiffert, P. Henning, P. Rupp, S. Zherebtsov, P. Hommelhoff, M. Kling, and T. Fennel, "Trapping field assisted backscattering in strong-field photoemission from dielectric nanospheres," J. Mod. Opt. **64**, 1096–1103 (2017).

37. L. Seiffert, F. Süßmann, S. Zherebtsov, P. Rupp, C. Peltz, E. Rühl, M. F. Kling, and T. Fennel, "Competition of single and double rescattering in the strong-field photoemission from dielectric nanospheres," Appl. Phys. B **122**, 101 (2016).